Ocean Engineering 190 (2019) 106426

Contents lists available at ScienceDirect

Ocean Engineering

journal homepage: www.elsevier.com/locate/oceaneng

Investigations on the vertical water-entry of a hollow cylinder with deep-closure pattern

Yu Hou, Zhengui Huang *, Zhihua Chen **, Zeqing Guo, Yuchuan Luo

National Key Laboratory of Transient Physics, Nanjing University of Science and Technology, Nanjing, 210094, China

ARTICLE INFO

Keywords:
Water entry
Hollow cylinder
Cavity evolution
Jet flow
Deep closure

ABSTRACT

The vertical water-entry of a low-speed hollow cylinder is studied numerically and experimentally in this work. The special flow characteristics of the hollow cylinder during the water entry have been revealed and discussed. Different from water entry of typical solid bodies, a through-hole jet with a bubble attached at the top forms at the impact stage, and the deep closure occurs around the circumference of the through-hole jet, and the secondary jet generated during the pinch-off has the shape of a hollow thin cylinder. Moreover, its head cavity includes both external and internal parts, and the internal cavity is more complicated and instable. The reasons for above differences have also been explained and discussed. Furthermore, the numerical results agree well with corresponding experimental data.

1. Introduction

Water entry is one of complicated events including cavity evolution, multiphase flow and impact etc., which exists extensively not only in natural fields, such as the basilisk lizard walking on water (Glasheen and McMahon, 1996), stones skipping (Clanet et al., 2004), and diving sports, but also in practical fields, such as bouncing bomb and aerial torpedo (Truscott, 2009; G. Pan and K. Yang, 2014), even some special application involved in seaplane landing (Von Karman, 1929), aerospace structures recovery from the sea (Seddon and Moatamedi, 2006) and airdropping sonobuoy (Liu and Wang, 2011) etc. Therefore, it attracts many researchers to study these problems.

The investigations on the water-entry of solid objects begin at the end of the 19th century. Worthington (1882) captured those phenomena experimentally such as air-entraining cavity and water splash during the vertical water-entry of rigid spheres with the use of single-spark photography. Later, further study about the effects of extensive parameters including vertical entry velocity (Wang and Guedes Soares, 2014), atmospheric pressure (Gilbarg and Anderson, 1948; May 1952; Marston et al., 2016) and surface characteristics (Aristoff and Bush, 2009) on the entraining cavity evolution and resistance coefficients were carried out progressively. Afterwards, the entry structures and conditions of objects are expanded to enrich such phenomena. The water entry of cylindrical projectiles with different nose shapes (Guo, 2012; He, 2012), disks (Bergmann et al., 2009), spinning spheres (Truscott and Techet, 2009) are also studied. Truscott et al. (2014) summarized the research results of many studies including both the entraining cavity of low-speed bodies, and the supercavitation of high-speed projectiles.

The water entry of hollow cylinder has not been investigated directly. However, flow fields characteristics of objects with a hole or an intake duct have also been investigated, such as the semi-closed cylinder (Lu et al., 2016), high speed crafts with artificial air cavity (Edward and Wukowitz, 1968; Ou et al., 2010; Cucinotta et al., 2017), the underwater vehicle with ventilation (Jiang et al., 2018) etc. Compared to solid objects, the water entry and motion of hollow structures in water can lead to more complicated flow fields, which need better understanding. Tseitlin (1959) first proposed that the solution of the plane problem of a flow past two flat plates can be extended to flow past the disc with a hole. Deinekin (1994) numerically solved the problem of axisymmetric flow past a ducting cavitator. Savchenko (2012) studied experimentally the resistance characteristics of a disc cavitation with different apertures using a water tunnel and obtained the relationship between the drag coefficient and the added mass. On the other hand, Gokcay et al. (2004) confirmed the concept of artificial air cavity for high-speed craft based on the tank testing method. An experimental study of air-ventilated cavities using a simplified hull model has been carried out by Matveev et al. (2009). Some investigations have been conducted on the field of water entry. Lyu et al. (2015) experimentally investigated the

* Corresponding author.
** Corresponding author.
E-mail addresses: hzgkeylab@njust.edu.cn (Z. Huang), chenzh@njust.edu.cn (Z. Chen).

https://doi.org/10.1016/j.oceaneng.2019.106426
Received 31 May 2019; Received in revised form 15 August 2019; Accepted 7 September 2019
Available online 17 September 2019

displacements and trajectories of both the solid and hollow cylinders after their horizontally falling into a water flow. They found that the trajectories of the hollow cylinder collapse easily at the initial stage of submerging in water.

This present work is carried out based on the application background of using hollow projectiles to hit underwater objects. As we know that the hollow projectiles have strong penetration ability and low flow resistance in the air (Huang et al., 2013; Zhao et al., 2019). However, there are no investigations directly published on the flow evolution of the water-entry of a hollow projectile. Its fundamental pattern of the cavity evolution and ballistic trajectories need to be revealed clearly, which is also important for understanding the slamming of high-speed crafts with holes. Therefore, in this paper, the vertical water-entry of a hollow cylinder with a low entry speed is firstly studied to reveal the fundamental flow characteristics, which is important for future study on such phenomenon with different entry conditions.

This paper is organized as follows: Section 1 is the introduction. The experimental setup is provided briefly in Section 2. The numerical method is introduced in Section 3, which describes the VOF multiphase model, the realizable k-ε turbulence model and the dynamic grid generation. Section 4 refers to the results and discussions, which consists of 4 subsections. Section 4.1 provides the numerical validations of our experimental and numerical results. In Section 4.2~4.4, details of the flow field characteristics including cavity evolution, deep closure, the through-hole jet formation and the moving characteristics of the hollow cylinder are discussed and analyzed. Finally, the conclusion is shown in Section 5.

2. Experimental setup

The experimental system is illustrated in Fig. 1, which is mainly composed of a water tank, a high-speed camera, a lifting bracket, a launch platform, a lighting system and a computer. The water tank (1.0 m × 0.7 m × 1.0 m) is made of smooth glass with high transparency. The launch platform with an electromagnet to attract the hollow projectile is fixed above the water tank. When the electric current is cut off, the hollow projectile falls with an equal initial speed, and its entry speed (v_0) can be adjusted by modifying the height of the platform.

The cavity evolution is captured by a high-speed Phantom camera, and the software is used to handle the images and some data processing. The frame rate is chosen as 2000fps with the image resolution of 1280 × 800 pixels and the exposure time is 20 μs. Due to the high frame rate and the short exposure time, two 2600 W spotlights are placed behind and beside the tank to ensure the clarity of captured images.

As shown in Fig. 2, the hollow cylinder of the present experiment is made of steel ASTM1045 with a density ratio of $\rho_s/\rho_w = 7.85$, where ρ_s is the density of the hollow cylinder and ρ_w is the density of water. Its geometric parameters are shown in Table .1. The tap water with a temperature of 15 °C is used in the experiment and the water depth is 0.8 m. To calibrate the real size in the images, an accurate coordinate paper is posted on the tank background as the reference frame to measure the position coordinates of the hollow cylinder. The edge detection algorithm based on the Sobel operator in MATLAB is used to obtain the hollow cylinder location in Fig. 1(a), where the origin of ordinate x and the trigger time are taken to be the water-entry location and the water-entry impacting time, respectively.

The displacement of the hollow cylinder can be translated by the pixel coordinate of images based on the calibration. The velocity of the cylinder could be represented by the average velocity of two sequential images obtained by the high-speed camera. Similarly, the acceleration which is defined as $a = (v_t - v_0)/\triangle t$ can be calculated. In this work, the hollow cylinder entered the water with the entry velocity of $v_0 = 2.84$ m/s and the Froude number is $Fr = v_0/\sqrt{gD_c} = 7.14$, where D_c ($D_c = \sqrt{D^2 - d^2} = 16.1$mm) is the characteristic length based on both the inner and outer diameter. The hollow cylinder is released at the same height for six times and the averaged data are used for discussion, which ensures the phenomenon reproducibility and the measuring accuracy. The maximum measurement error is estimated to be less than 5%.

3. Numerical method

3.1. Computational equations and turbulence model

The VOF model in the form of Reynolds-averaged Navier-Stokes equations are employed for describing the vertical water-entry cavities. The continuity equation of the mixture flow is

$$\frac{\partial \rho_m}{\partial t} + \frac{\partial (\rho_m u_j)}{\partial x_j} = 0 \tag{1}$$

Where ρ_m=(1-α_{water}) ρ_a+α_{water} ρ_w represents the mixture density. ρ_a and ρ_w refer to the air and water density, respectively.

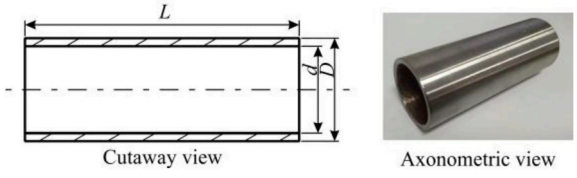

Fig. 2. Schematic of the water-entry cylinder.

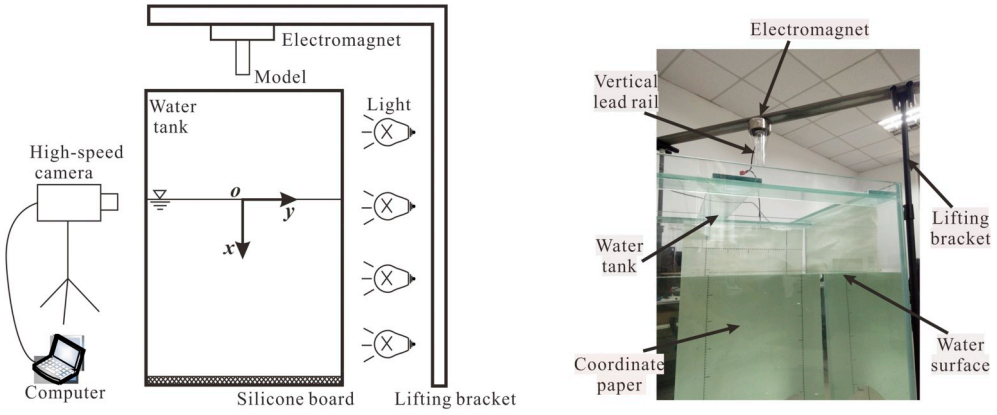

Fig. 1. (a) Schematic of the experimental setup and (b) A image of the water tank.

Table 1
Details of the hollow cylinder.

D/mm	d/mm	d/D	L/mm	M/kg
30.0	25.3	0.84	80.0	0.128

The momentum equations are

$$\frac{\partial \rho_m u_i}{\partial t}+\frac{\partial\left(\rho_m u_i u_j\right)}{\partial x_j}=\rho_m g_i-\frac{\partial P}{\partial x_i}+\frac{\partial}{\partial x_j}\left[\left(\mu_m+\mu_t\right)\left(\frac{\partial u_i}{\partial x_j}+\frac{\partial u_j}{\partial x_i}\right)\right] \tag{2}$$

where g_i represents the gravity acceleration in x_i coordinate. P is the mixture pressure. μ_m (μ_m=(1-α_{water}) μ_{air} +α_{water} μ_{water}) denotes the mixture dynamic viscosity coefficient and μ_t refers to the turbulent viscosity.

The two-equation k-ε turbulence model is used to close the viscous equation. And the turbulent kinetic transport equation (k) is given as

$$\frac{\partial(\rho_m k)}{\partial t}+\frac{\partial(\rho_m k u_i)}{\partial x_i}=\frac{\partial}{\partial x_i}\left[\left(\mu+\frac{\mu_t}{\sigma_k}\right)\frac{\partial k}{\partial x_i}\right]+G_k+G_b-\rho_m\varepsilon-Y_M+S_k \tag{3}$$

The transport equation of the dissipation rate of energy of the turbulent flow (ε) is written as

$$\frac{\partial(\rho_m \varepsilon)}{\partial t}+\frac{\partial(\rho_m \varepsilon u_i)}{\partial x_i}=\frac{\partial}{\partial x_i}\left[\left(\mu+\frac{\mu_t}{\sigma_\varepsilon}\right)\frac{\partial \varepsilon}{\partial x_i}\right]+\rho C_1 S\varepsilon-\rho C_2\frac{\varepsilon^2}{k+\sqrt{\nu\varepsilon}}+C_{1\varepsilon}\frac{\varepsilon}{k}C_{3\varepsilon}G_b+S_\varepsilon \tag{4}$$

Where $C_1=\max\left[0.43,\frac{\eta}{\eta+5}\right]$, $\eta=S\frac{k}{\varepsilon}$, $S=\sqrt{2S_{ij}S_{ij}}$.

In these k-ε equations, $G_k=\mu_t S^2$ and $G_b=\beta g_i\frac{\mu_t}{Pr_t}\frac{\partial T}{\partial x_i}$ represent the generation of turbulence kinetic energy due to the mean velocity gradients and buoyancy, respectively. The default value of Pr_t is 0.85 and $\beta=-\frac{1}{\rho}\left(\frac{\partial \rho}{\partial T}\right)_p$. $Y_M=2\rho k\varepsilon/\gamma RT$ represents the contribution of the fluctuating dilatation incompressible turbulence to the overall dissipation rate. C_2 and $C_{1\varepsilon}$ are constants. σ_k and σ_ε are the turbulent Prandtl numbers of k and ε, respectively. In this work, $C_2=1.9$, $C_{1\varepsilon}=1.44$, $\sigma_k=1.0$ and $\sigma_\varepsilon=1.2$ are the default values. Meanwhile, no extra source terms of S_k and S_ε are defined.

The above time-dependent governing equations are discretized by the finite volume method, and the SIMPLE scheme is used to solve the pressure-velocity coupling algorithms. The second-order upwind scheme is applied for discretizing the convection terms and the central-differenced for the diffusion term of the momentum equations. The PRESTO scheme is adopted for the pressure interpolation. The Geo-Reconstruct scheme is employed for solving the transport equation for the volume fractions.

3.2. Computational domain and grid generation

In this work, an axisymmetric two-dimension plane is chosen as the computational domain for the simulation. The entire domain size is $15D \times 45D$ and is shown in Fig. 3. The stationary wall is chosen for both side and bottom boundary. The top boundary is set as pressure-inlet. The operating pressure P_0 is taken to be the standard atmospheric pressure 101325Pa. The hollow cylinder falls at the height of $1.25D$ with the initial velocity of 2.707 m/s to obtain the vertical water-entry speed of 2.84 m/s. The origin of x coordinate and starting time are taken to be the center of entry location and the impact moment. The water depth is $30D$.

The structured mesh is created for the whole domain as shown in Fig. 4(a). The area around the hollow cylinder and the interface of two-phase flow are refined to improve the numerical accuracy and is shown in Fig. 4(b). The dynamic layer method is used to update the mesh. When the grid size h_i is compressed or stretched to a certain value, the mesh splits or collapses following the layering rules of Eqs. (5) and (6), which is defined as:

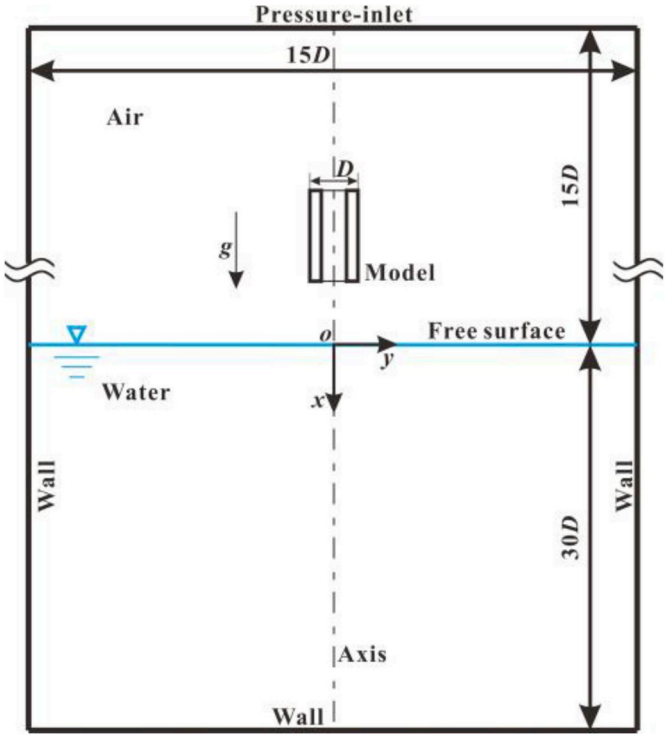

Fig. 3. Schematic of the computational domain and boundary conditions.

$$h_i>(1+\alpha_s)\cdot h_{ideal} \tag{5}$$

$$h_i<\alpha_c\cdot h_{ideal} \tag{6}$$

where h_{ideal} is the ideal cell height, α_s is the layer split factor and α_c is the layer collapse factor. In this work, $\alpha_s=0.1$, $\alpha_c=0.04$.

A mesh dependency study has been conducted and four different grid levels with correspondingly coarse (0.5 million), medium (0.7 million), fine (0.9 million) and finer (1.2 million) grid are examined. Their predicted depths (x) versus time are shown in Fig. 5. A computer workstation with 16 processors is used to perform the whole simulations, the time step is set up as 5×10^{-6}s to ensure the convergence of the simulations, and it takes about 168 hours. In addition, iterations are also required to make the solution converge at each time step.

As shown in Fig. 5, the differences of entry depths mainly come from later times. Considering both the accuracy and the computational resource cost in the present simulation, the grid number of 0.9 million is applied in the present work, and its non-dimensional distance (y^+) satisfies $y^+<25$ as shown in Fig. 6.

4. Results and discussions

4.1. Numerical validations

To validate the numerical method, the numerical results are compared directly with corresponding experimental results. The high-speed images of the water entry process of a hollow cylinder with vertical entry velocity, $v_0=2.84$ m/s, are shown in Fig. 7(a). Corresponding numerical results are shown in Fig. 7(b). Due to the opacity of hollow cylinder, the flow within the hollow cannot be observed. It is clear that both experimental and numerical flow results agree well with each other, and some special phenomena of hollow cylinder including the generation of jet, its top bubble evolution and the annular wake cavity can also be seen clearly and will be discussed later.

Following the discussions of May (1952) and Truscott et al. (2014), the water-entry cavity evolution of a hollow cylinder can also be divided

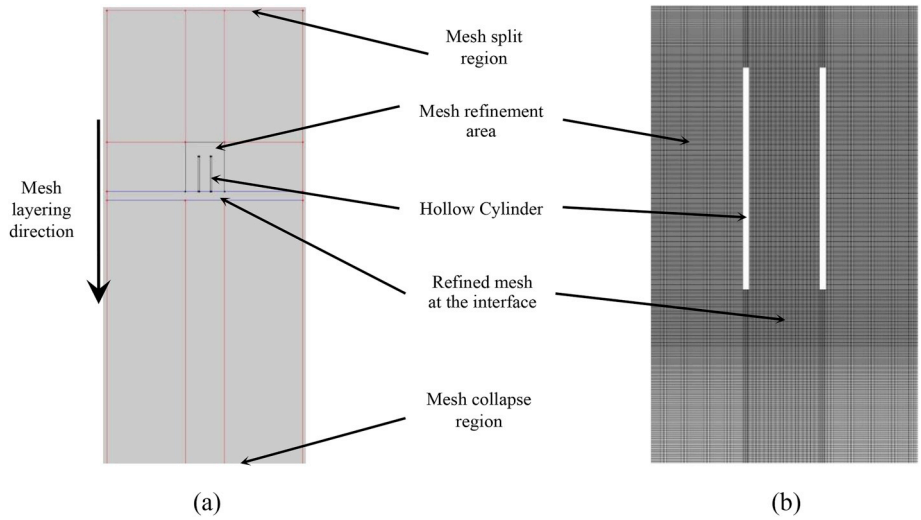

Fig. 4. Mesh structures of the computational domain. (a) the mesh block of the whole domain (b) the mesh around the hollow cylinder.

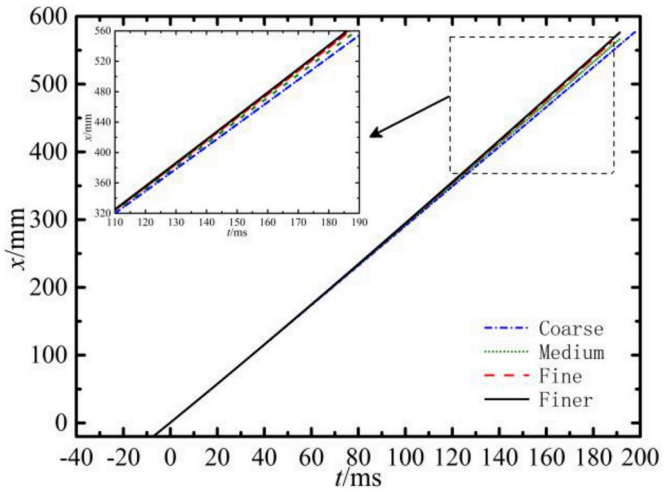

Fig. 5. Numerical results of the hollow cylinder depth variations with four different gird meshes.

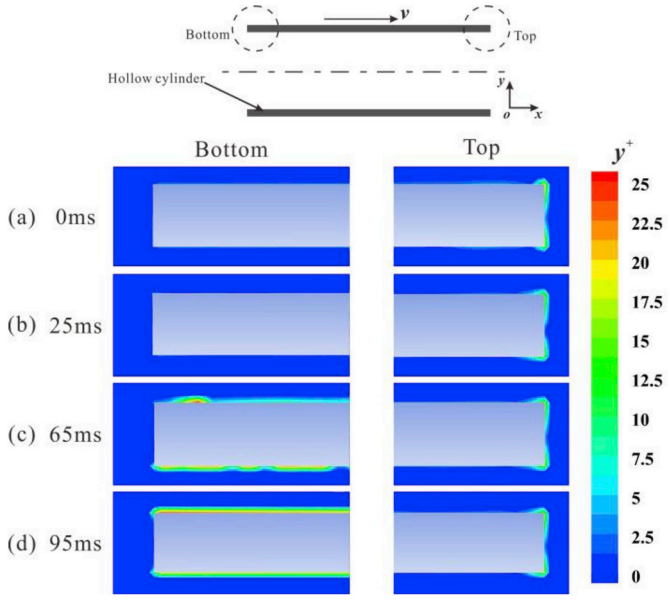

Fig. 6. Distribution of y^+ around the top and bottom of the hollow cylinder.

into four distinct stages: the impact stage, the open cavity stage with jets growth, the pinch-off stage and the sailing stage with cavity attached. The initial splash caused by the impact is almost symmetrical and the through-hole jet (induced by the hollow) forms (Fig. 7(b), $t = 5$, 15 ms). The cavity closure occurs at about $t = 65$ ms, and the values of the pinch-off depth for experiment and simulation are 2.66D (Fig.7(a)) and 2.52D (Fig. 7(b)), respectively, their maximum diameters of the attached cavity are 1.21D (Fig.7(a)) and 1.27D (Fig. 7(b)), respectively.

Moreover, comparisons of the experimental measurements and the numerical parameters of the depth x, the velocity v and acceleration a are shown in Fig. 8, which show that the numerical results have the same trend and almost the same values of corresponding experimental results. For the depth and velocity shown in Fig. 8(a)–(b), the experimental values are a little larger than that of the numerical results. These may be caused by the pixel resolution of the photos of the experiments. However, the maximum errors of them are only 5.38% and 8.68%, which is acceptable. In addition, Fig. 8(c) also shows the same varying trends of acceleration and the maximum error occurs at the impact time ($t = 0$ ms) and the pinch-off time ($t = 65$ ms) due to the high data saltation, which cannot be captured accurately in the experimental measurement. Therefore, we can see that the numerical predictions of the entry water of the hollow cylinder are compatible with the corresponding experimental measurements.

4.2. Flow characteristics of the entry cavity evolution

To illustrate the characteristics of flow fields of the entry cavity evolution, distributions of flow velocity contours and streamlines are shown in Fig. 9 and Fig. 10, the left half of each image refers to the velocity contours while the right denotes the streamlines. The impact, the open cavity ($t = 0$-35 ms) and the transitional period ($t \approx 40$ ms) are exposed in Fig.9, and Fig.10 displays the pinch-off and the sailing stage with cavity attached from 60 ms to 85 ms.

When the hollow cylinder impacts with the water interface, it transfers kinetic energy and makes water move (Fig. 9(a)), then the interface shape is modified and a cavity forms. The flow in front of the cylinder head is divided into two regions: the surrounding and the pierced regions ($t = 5$ ms, Fig.9(b) and Fig.7). The surrounding flow around the interface forms a transparent and smooth water curtain around the cylinder over the free surface, which is like a splashed crown. The subsurface flow keeps expanding to form an axisymmetric cone

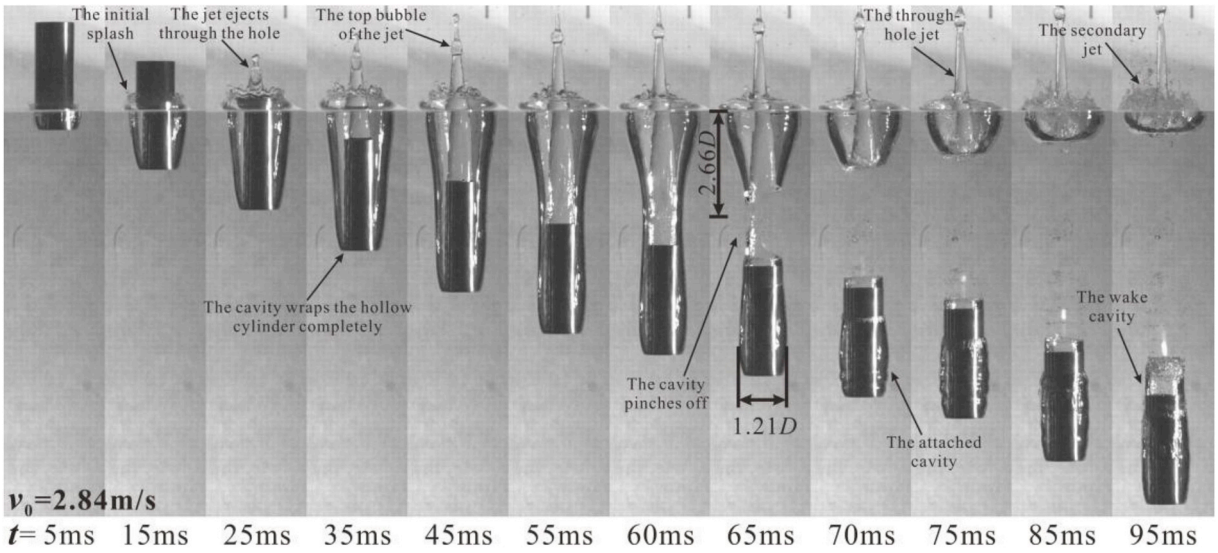

(a) Experimental photographs

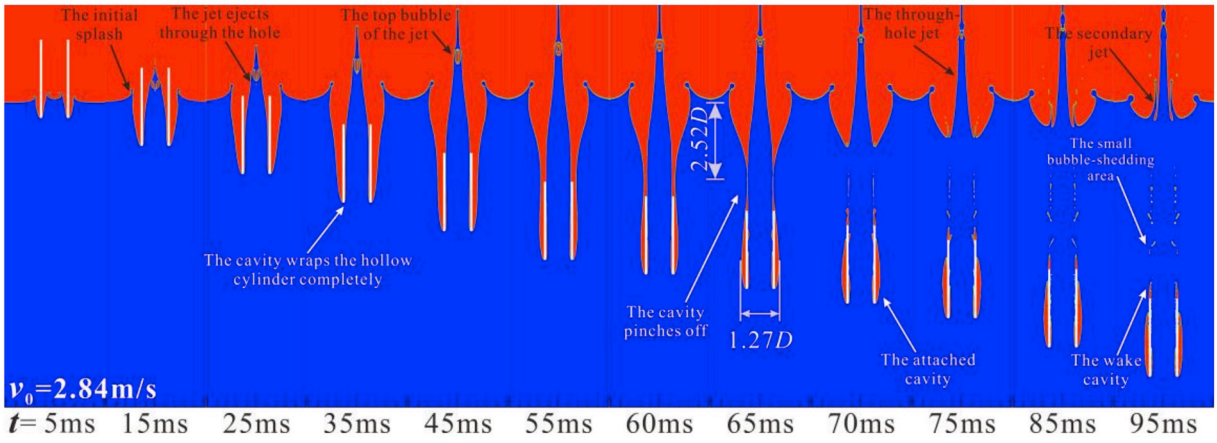

(b) Numerical results

Fig. 7. Comparing (a) experimental photographs (b) with numerical results for the vertical water-entry cavity of the hollow cylinder.

cavity that wraps the cylinder. Meanwhile, due to the low pressure of cavity, surrounding air is entrained into it and the velocity becomes high near the splash crown (Fig. 9(c)). On the other hand, the pierced flow moves upward along the inner wall of the hollow to form a through-hole cone jet with a bubble attached at its top, which is the special phenomenon for the water entry of a hollow cylinder ($t \geq 25$ ms, Fig. 7(a)–(b) and Fig. 9(e)-(f)).

The open cavity stage includes the expansion, extension, and shrink of the entry cavity. After the formation of a splashed crown and the through-hole jet, the entry cavity keeps expanding, and satisfies the principle of independence of cavity expansion. On the other hand, the expansion lets the internal pressure of cavity low and entrains surrounding air. When the expanding speed of cavity wall becomes zero, ($t = 35$ ms, Fig. 9(d)), it moves inwards and leads to the formation of a vortex outside the cavity wall (Fig. 9(e)–(f)).

During the shrink process of the cavity, a deep closure occurs at about $t = 65$ ms (Fig.10(b), Fig.7). However, the pinch-off of the hollow cylinder cavity appears along the circumference of the through-hole jet, which is different with the traditional deep closure of a solid cylinder with cavity shrinking and collapsing to a point (May 1952; He, 2012; Truscott et al., 2014). Meanwhile, the cavity is separated into two parts, one is connected to the atmosphere and jet, and it keeps moving up to the interface, the other is attached to the cylinder and moves downward (Fig. 7 and Fig.10(a)–(c)). During the early pinch-off, the maximum speed of the air within these two cavities can be several times larger than the water entry speed.

After the cavity closure, the extrusive through-hole jet keeps moving up toward the surface with the cavity attached at its bottom, and when the cavity is close to the free surface, a secondary hollow jet generates at the bottom ($t = 75$ ms, Fig. 10(d)) and its diameter is equal to that of the cylinder. This is also different from the Worthington jet (Mckown, 2011) formed by the cavity closure of the typical solid bodies. The secondary jet has the shape of a hollow thin cylinder, and its moving speed increases gradually and then decreases under the action of gravity ($t = 95$ ms, Fig.7(b) and Fig.10(e)). In addition, the downward cavity shrinks ($t = 70$ ms, Fig. 10(c)), and the cylinder starts its free fall sailing.

In the sailing stage, the downward cavity is attached to the cylinder. Its flow streamlines just like magnetic field lines (Fig. 10(d)) that move steadily along with the attached cavity due to the water being pushed away at the head and move back around the tail of the cylinder. At the same time, the downward cavity breaks into two portions (head and tail) at $t \geq 65$ ms (Fig. 10(b)–(e) and Fig.7). The head portion includes both external and internal bubbles, while the tail one is attached to the cylinder bottom and is separated from the head bubble. The wake cavity keeps shedding and a series of small bubbles are observed within the wake flow at $t = 85$ ms (Fig.10(d) and Fig.7(b)).

To further investigate the flow characteristics of the sailing stage, the vorticity contours ($\Omega_z=(\partial V_y/\partial x-\partial V_x/\partial y)/2$, left half) and the mixture

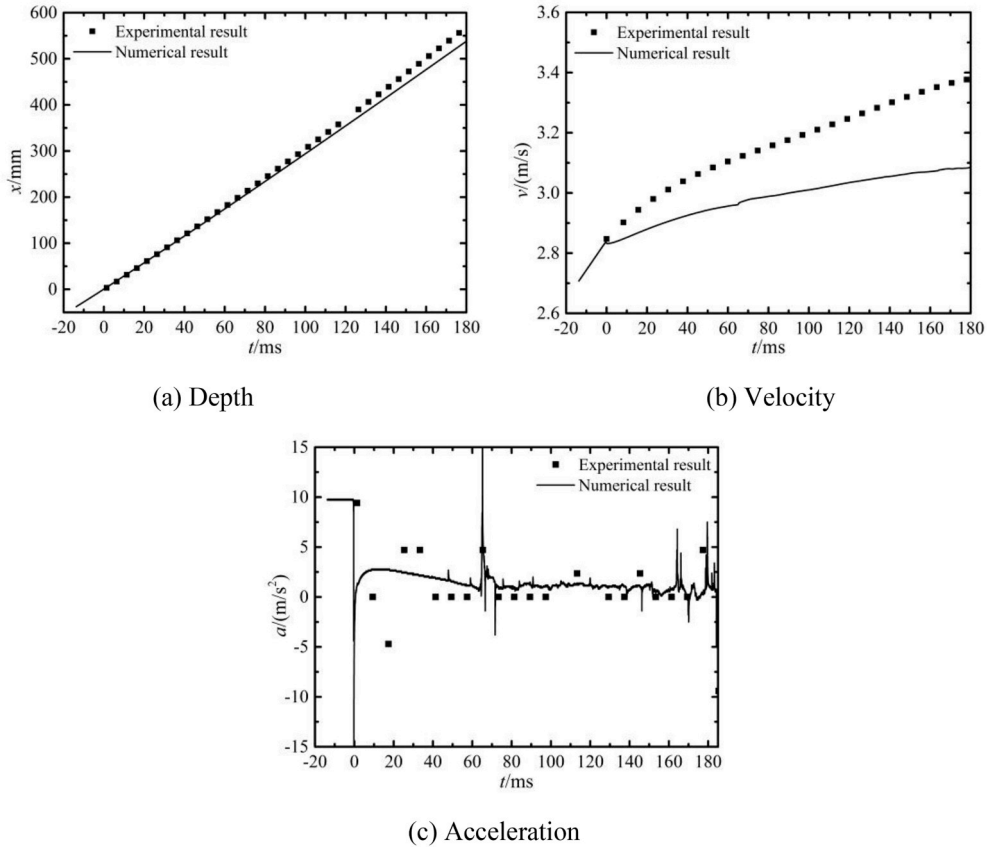

Fig. 8. Comparisons of (a) depth x, (b) velocity v and (c) acceleration a between the experimental and numerical results with the entry velocity of 2.84 m/s.

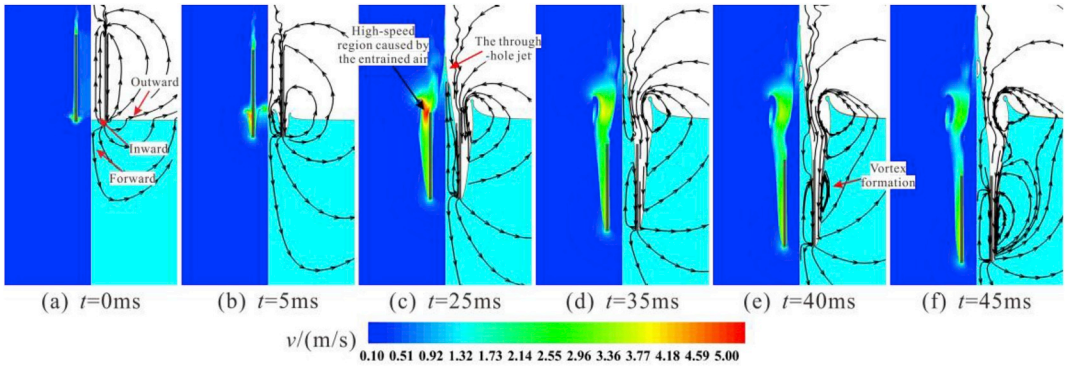

Fig. 9. The velocity field and the flow streamlines at typical moments from 0 ms to 45 ms in the simulation with the entry velocity of 2.84 m/s.

volume fraction with embedded streamlines (right half) of the numerical results, and comparison of the experimental photograph at $t = 95$ ms are presented in Fig. 11. As we can see that, both experimental and numerical cavity diameters have the same maximum value of 1.29D. However, their head cavity lengths are somewhat different, 2.28D and 2.18D, respectively. And the same with that of their lengths of wake cavity, they are 0.59D and 0.56D, respectively. But the discrepancies between them are only 4.39% and 5.08%, which are totally acceptable.

From Fig. 11, the attached head cavity and its pattern along with the outer and inner wall of the cylinder can be observed clearly (Fig. 11(b)). Fig. 11(c) shows the zooming in of the internal cavity, where some droplets are observed to stick along both sides of the cylinder. Based on the streamlines distribution, we deduce that the droplets are induced by the immersion of the backflow. Fig. 12 shows the head cavity evolution and bubbles generating process. The head cavity is unstable (Fig. 12). The internal cavity forms when the head cavity touches the inner wall at $t = 55$ ms (Fig. 12(b)), and it is a typical mixing layer, under the action Kelvin-Helmholtz instability, its interface becomes instable, and rolls into small eddies with air included and bubbbles separating from the wall. In fact, the external cavity is just like the internal one, and their shedding bubbles will merge with wake cavity to form the wake flow. After generated, the bubble moves up toward the tail, and its shape keeps changing during the moving process (Fig. 12(c)–(e)).

Due to the random disturbances, the location of the first rolled bubble (I) is not fixed, and it fluctuates with the evolution of the head cavity. The variations of both internal and external locations can be found in Fig. 13. It is clear that the fluctuating frequency of internal cavity is almost three times larger than that of external one, and its cavity size is smaller, therefore, it is more instable.

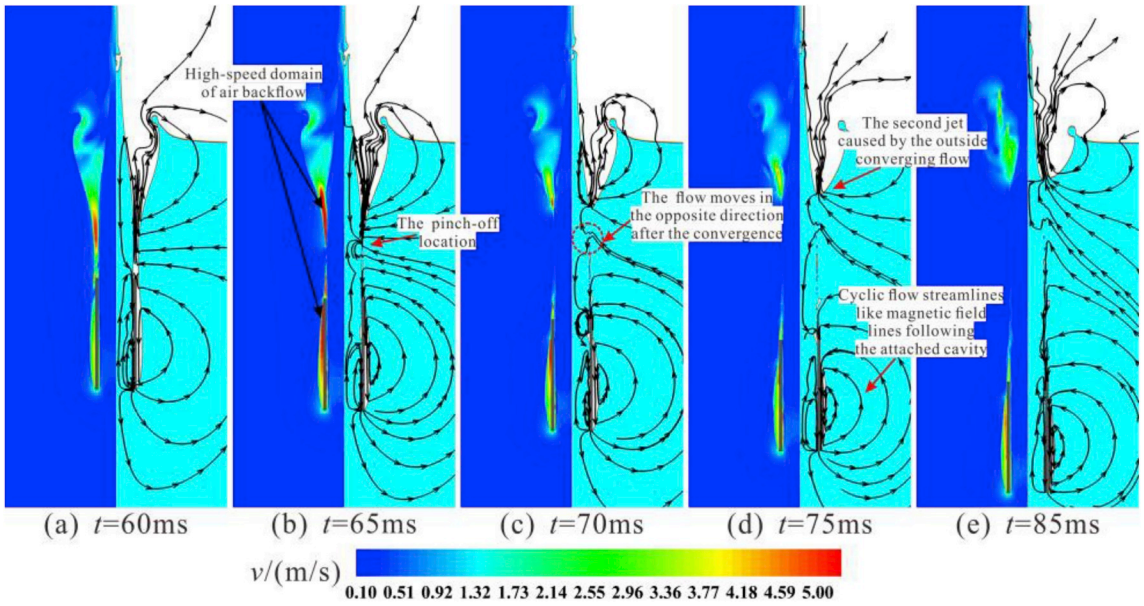

Fig. 10. The velocity field and the flow streamlines at typical moments from 60 ms to 85 ms in the simulation with the entry velocity of 2.84 m/s.

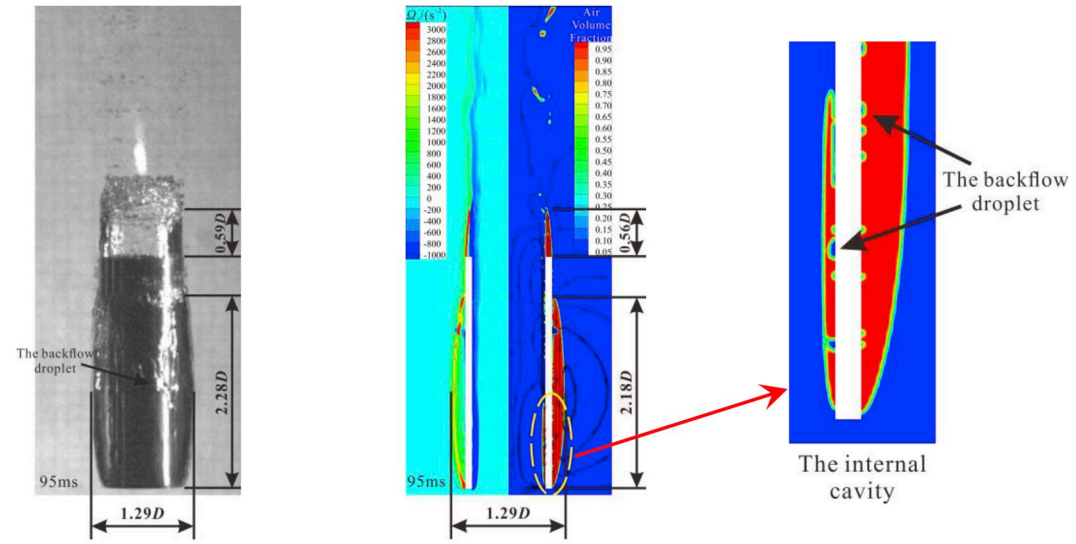

Fig. 11. Comparison of the attached cavity between numerical and experimental results at $t = 95$ ms

4.3. Evolution of the through-hole jet

To investigate the through-hole jet characteristics, the contours of air volume fraction at the early stage of water entry are shown in Fig. 14. It is clear that the jet is induced by the hollow, and it includes a top bubble and the liquid column, which is similar to the cavitation flow in the orifice (Ramamurthi and Nandakumar, 1999).

As shown in Fig. 14(a) and (h), when the cylinder impacts the water surface, the high-pressure region occurs at the impact area and transfers the kinetic energy from the hollow cylinder to the water. At the same time, an area with inward oblique high-pressure gradient forms near the inner cylinder wall, which makes the flow obtain high oblique upward velocity, therefore, a through-hole jet with concave head forms inside the hollow (Fig. 14(b)).

With time goes on, the head edge of the through-hole jet will collide at the axis due to their high oblique velocity, the air around the head center is encircled by the rolled edge and a bubble is generated (Fig. 14 (c)). At the same time, the collision of head edge induces two new small jet flows with opposite direction. One of them moves upward and turns into the head of the through-hole jet, and the other moves downward, it passes through the bubble, impacts and merges with the through-hole jet. The bubble along with the through-hole jet keeps moving upward, and at about $t = 15$ ms (Fig. 14(d)), the jet moves out of the water surface. The bubble in the head of through-hole jet can also be seen by corresponding experimental images (Fig.14(g) and Fig.7(a)).

Both the numerical and the experimental displacements (x) of the through-hole jet are shown in Fig. 15. Based on the numerical results, the evolution of upward jet can be divided into three stages: jet formation, bubble formation and jet stretch. The jet formation is caused by the impact of the cylinder with water and its upper speed is not very large,

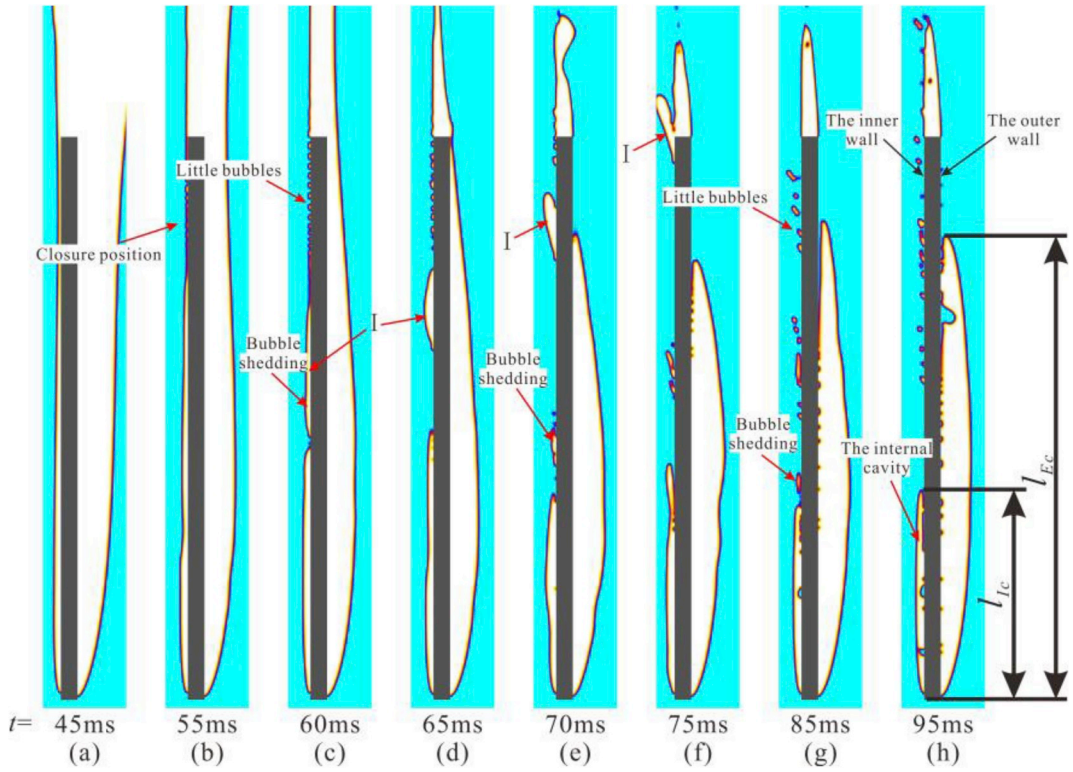

Fig. 12. The bubble generating process.

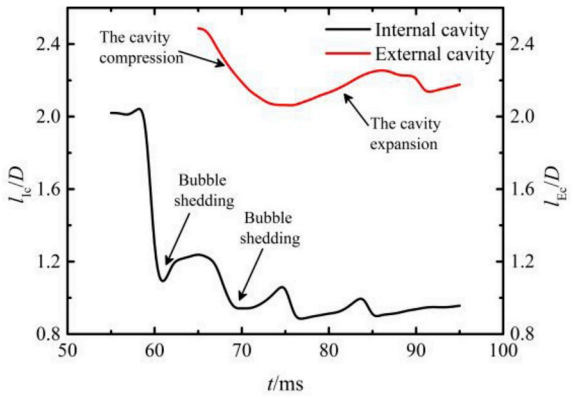

Fig. 13. The variations of the internal and external locations.

then, the bubble is formed due to the rolling up of head edge and lasts from 10 to 15 ms. At this time, its moving speed is the largest due to the generation of the small upward jet. The free jet stretch stage lasts very long and its upward speed is almost constant at t ≤ 48 ms.

The experimental data are taken from $t = 18$ ms since the through-hole jet can only be visualized when the jet moves out of the hollow cylinder. It is clear that the numerical displacement has the same rising trend as that of the experiment. However, the experimental results are a little smaller, since the fact that there are some droplets keep separating from the jet tip in the experiments and have not been counted in.

4.4. Moving characteristics of the hollow cylinder

The main parameters of the moving hollow cylinder during water entry are shown in Fig. 16-18, which mainly include the velocity v, acceleration a and drag coefficient C_d. The velocity v and the acceleration a are obtained from the numerical results directly. The drag coefficient is defined as:

$$C_d = F/(0.5\rho_w v^2 A) \tag{7}$$

and the total resistance is defined as:

$$F + Mg = Ma \tag{8}$$

where $A = lD_c/2$ is the characteristic area of the hollow cylinder and $l = 1$ is the unit length based on the 2D simulation.

The variation of the cylinder velocity can be observed in Fig. 16, and there are two saltation points with sharp modifications of the gradient at the entry and deep closure points. The velocity modification can also be divided into three stages, the free fall stage, the open cavity stage and the free sailing stage. Corresponding stages can also be clearly seen in Fig. 17. The two saltation points both have high acceleration gradients, but one is negative and the other is positive, which means that the water entry impact produces a great drag on the cylinder and it is on the contrary for the deep closure of the cavity. Except that, the acceleration remains almost constant during the free sailing stage, except that there are some fluctuations caused by the shedding bubbles and vortices.

The variation of the drag coefficient during the water entry process can be seen in Fig. 18. Except for the large water impact force (t = 0 ms) and cavity closure thrust (t = 65 ms), the cylinder drag is almost constant. However, the zoom-in picture of force shows that there are some small fluctuations, which can be explained by Fig. 19.

The contours of air volume fraction and the second invariant Q $\left(Q = \frac{1}{2}\left[\left(\frac{\partial v_x}{\partial x}\right)^2 + \left(\frac{\partial v_y}{\partial y}\right)^2\right] + \frac{\partial v_y}{\partial x}\frac{\partial v_x}{\partial y}\right)$ of the wake flow ($t = 140$ ms) are both shown in the upper and down side of Fig. 19, respectively. It is clear that there are vortices and small bubbles keep shedding away from the cylinder tail, which make the local pressure of cylinder fluctuate and induce the variation of cylinder drag.

As shown in Figs. 17–18, there is a large thrust generated during the deep closure of the cavity. The reason can be found in both in Fig. 20 and

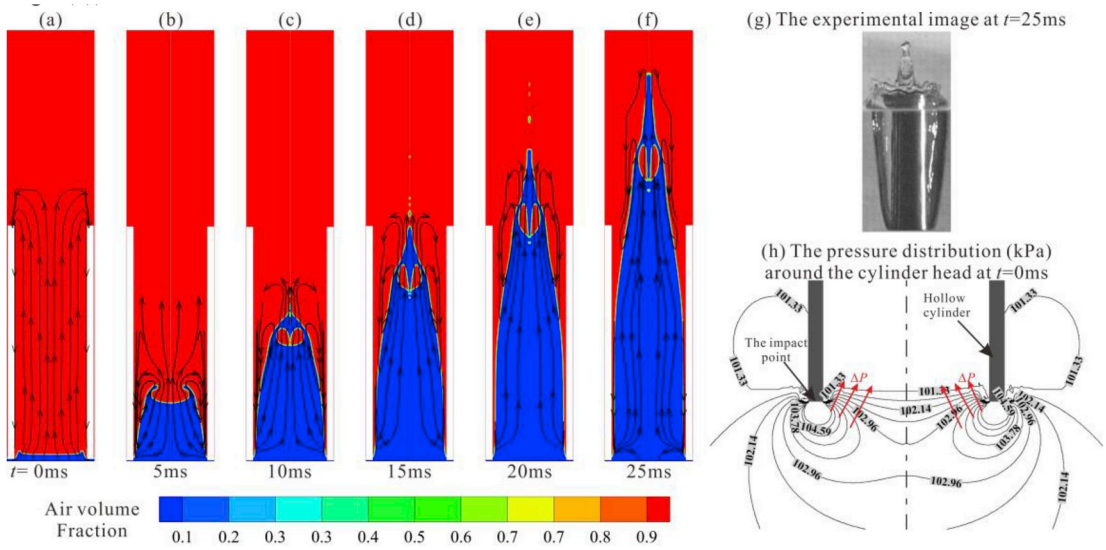

Fig. 14. The formation of the through-hole jet and the top bubble.

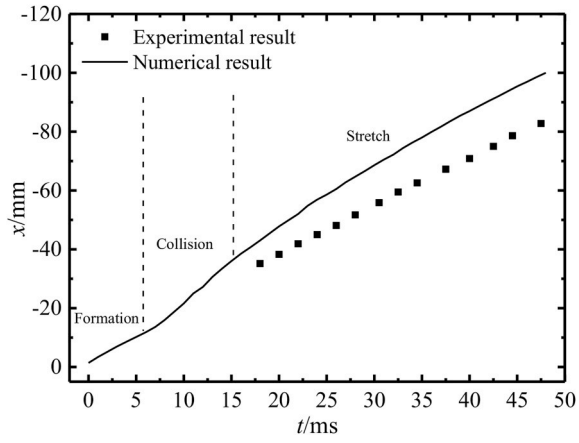

Fig. 15. Comparison of the numerical and experimental trajectories of the through-hole jet.

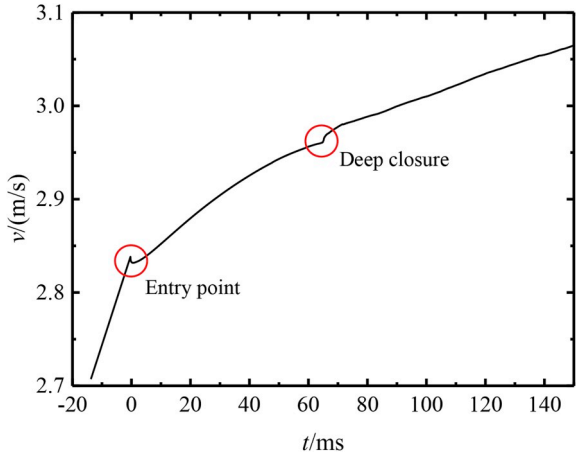

Fig. 16. The numerical velocity of the hollow cylinder with the vertical water-entry speed $v_0 = 2.84$ m/s.

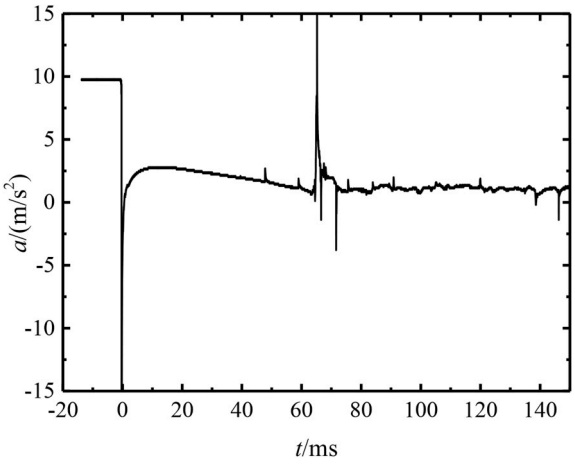

Fig. 17. The numerical acceleration of the hollow cylinder with the vertical water-entry speed $v_0 = 2.84$ m/s.

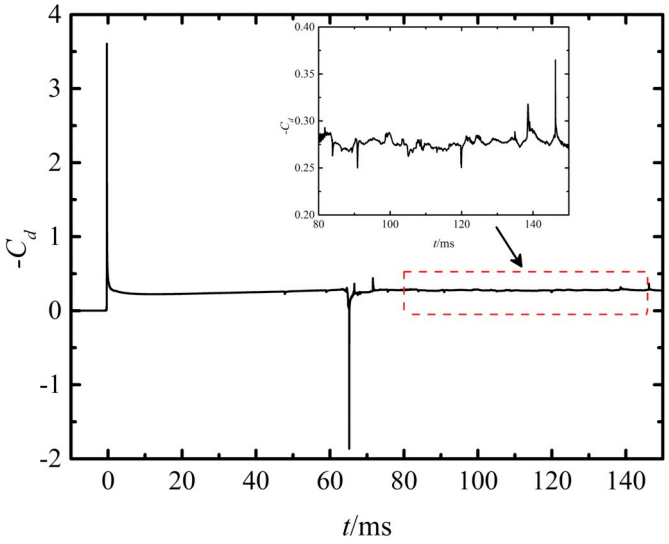

Fig. 18. The numerical drag coefficient of the hollow cylinder with the vertical water-entry speed of $v_0 = 2.84$ m/s.

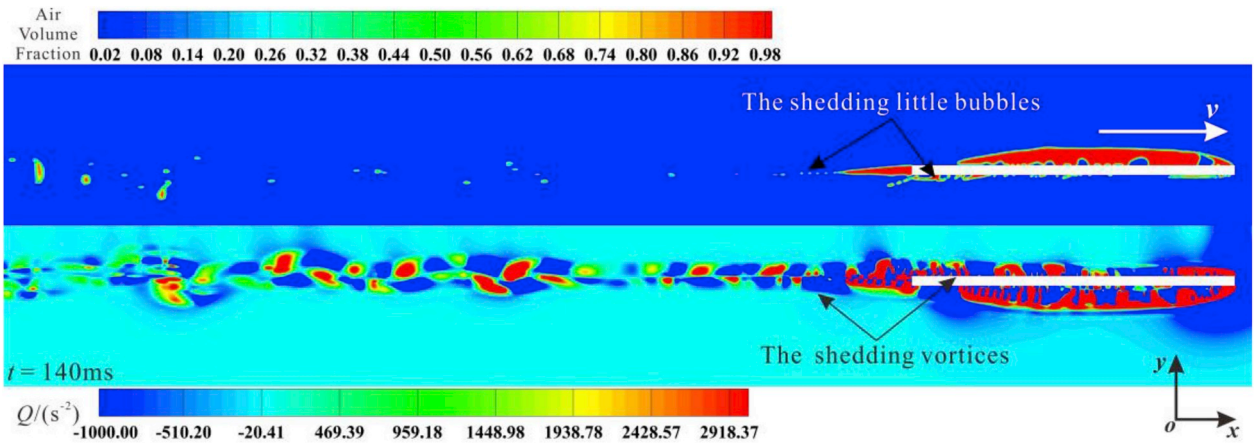

Fig. 19. Air volume fraction (upper) and the second invariant Q (lower) distribution of the wake flow at $t = 140$ ms

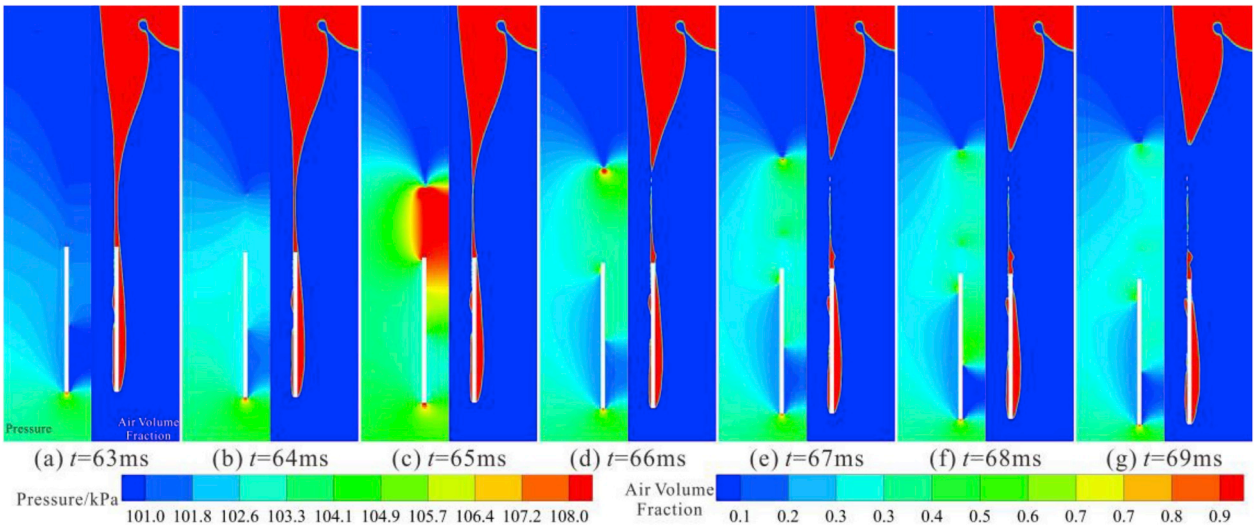

Fig. 20. The flow fields around the hollow cylinder during the pinch-off process. Left half: Pressure contours; Right half: Air volume fraction.

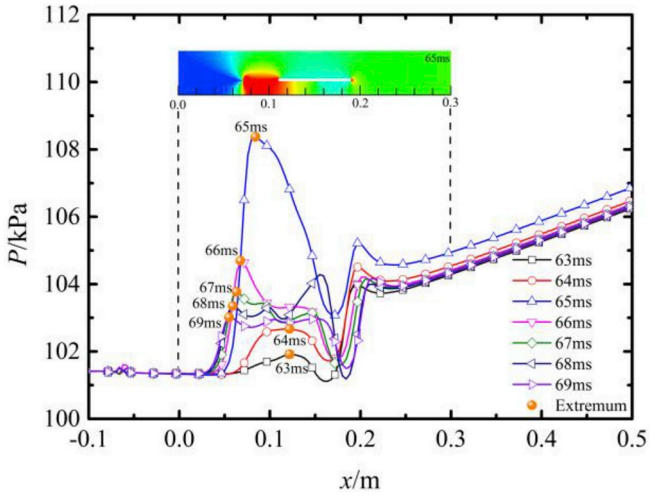

Fig. 21. The flow pressure variations along the axis of the cylinder during the pinch-off process.

Fig. 21, which illustrates the distributions of the pressure contours of the flow fields (left half) and the pressure variation line along the cylinder axis during the pinch-off process. Usually, the high-pressure location appears at the cylinder head (Fig. 20(a)–(g)). However, when the pinch-off occurs, two opposite jets form. The upper one is the cause of a secondary hollow jet as shown in Fig. 7(g), while the lower one moves downward and acts at the cylinder bottom that makes the pressure in this area raise quickly (Fig.20(c) and Fig.21, $t = 65$ ms), which acts actually a large thrust on the cylinder and accelerates it abruptly.

5. Conclusions

In this paper, the vertical water-entry of a low-speed hollow cylinder is studied. Both of our numerical and experimental results agree well with each other. The process of the whole water entry, including the flow characteristics, the evolution of the through-hole jet and the moving features of the hollow cylinder etc. are captured. The main findings of this work are concluded as follows:

(1) The water entry of hollow cylinder can also be divided in to four stages just like the entry process of solid bodies: the impact, the open cavity, the deep closure and the free sailing stage. However, for the hollow cylinder, the through-hole jet forms due to the hollow at the impact stage, and the deep closure of the cavity

occurs along the circumference of the through-hole jet, the secondary jet which is generated during the pinch-off has the shape of a hollow thin cylinder. Moreover, during the sailing stage, the cylinder head cavity includes both external and internal portions and the internal cavity is more instable and its length fluctuates along the cylinder inner wall. All of above phenomena distinguish the water entry process of a hollow cylinder from the usual entry process of solid bodies.

(2) The through-hole jet induced by the hollow structure contains a bubble on its head, which is attributed to the rolling up of its head edge. The air is encircled during their collision process. At the same time, there are two small jets generated. One moves upward and becomes the head of the through-hole jet, and the other moves downward and across the bubble, it merges with the through-hole jet.

(3) The moving characteristics of the hollow cylinder during the whol water entry process are determined by two stages, the entry impact and deep closure. However, they have opposite effects on the cylinder moving. The impact of water produces a large drag on the cylinder and makes it transfer large kinetic energy to water, therefore, its velocity decreases quickly. During the deep closure, there is a large thrust generated due to the formation of a downward jet, which induces a big acceleration of the cylinder.

Acknowledgments

This work is supported by “the Key Laboratory Fund” No.61426040303162604004 and No.614260403041803, “the Fundamental Research Funds for the Central Universities” No.30917012101 and “the Postgraduate Research & Practice Innovation Program of Jiangsu Province” No.KYCX19_0259.

References

Aristoff, J.M., Bush, J.W.M., 2009. Water entry of small hydrophobic spheres. J. Fluid Mech. 619, 45–78.
Bergmann, R., Van Der Meer, D., Gekle, S., Van Der Bos, A., 2009. Controlled impact of a disk on a water surface: cavity dynamics. J. Fluid Mech. 633, 381–409.
Clanet, C., Hersen, F., Bocquet, L., 2004. Secrets of successful stone-skipping. Nature 427, 29.
Cucinotta, F., Guglielmino, E., Sfravara, F., 2017. An experimental comparison between different artificial air cavity designs for a planing hull. Ocean Eng. 140, 233–243.
Deinekin, P.Y., 1994. Cavity flow past flow passage bodies. Gidromekhanika 01, 74–78.
Edward, Wukowitz, 1968. High-speed Motorboat Hull, 14 May. U.S. Patent.. No. 3382833.
Gilbarg, D., Anderson, R.A., 1948. Influence of atmospheric pressure on the phenomena accompanying the entry of spheres into water. J. Appl. Phys. 19, 127–139.
Glasheen, J.W., McMahon, T.A., 1996. A hydrodynamic model of locomotion in the basilisk lizard. Nature 380, 340–342.
Gokcay, S., Insel, M., Odabasi, A.Y., 2004. Revisiting artificial air cavity concept for high speed craft. Ocean Eng. 31, 253–267.
Guo, Z., Zhang, W., Xiao, X., Wei, G., Ren, P., 2012. An investigation into horizontal water entry behaviors of projectiles with different nose shapes. Int. J. Impact Eng. 49, 43–60.
He, C.T., 2012. Low speed water-entry of cylindrical projectile. Acta Phys. Sin. 61, 134701.
Huang, Z.G., Li, Y.L., Chen, Z.H., Guo, Y.J., 2013. Numerical investigations on the drag and aerodynamic characteristics of a hollow projectile. Acta Armamentarii 34 (5), 535–540.
Jiang, Y., Bai, T., Gao, Y., Guan, L., 2018. Water entry of a constraint posture body under different entry angles and ventilation rates. Ocean Eng. 153, 53–59.
Liu, R., Wang, Y., 2011. Research of water-entry mechanical property of sonobuoy. Audio Eng. 35 (10), 59–62.
Lu, Z.L., Wei, Y.J., Wang, C., Sun, Z., Astronautics, S.O., 2016. An experimental study of water-entry cavitating flows of an end-closed cylindrical shell based on the high-speed imaging technology. Acta Phys. Sin. 65 (1), 014704.
Lyu, X., Wei, Z., Tang, H., New, T.H., Li, H., 2015. On the motion of a falling circular cylinder in flows after water entry. International Society for Optics and Photonics, p. 930233.
May, A., 1952. Vertical entry of missiles into water. J. Appl. Phys. 23, 1362–1372.
Matveev, K.I., Burnett, T.J., Ockfen, A.E., 2009. Study of air-ventilated cavity under model hull on water surface. Ocean Eng. 36, 930–940.
Marston, J.O., Truscott, T.T., Speirs, N.B., Mansoor, M.M., Thoroddsen, S.T., 2016. Crown sealing and buckling instability during water entry of spheres. J. Fluid Mech. 794, 506–529.
Mckown, J.M., 2011. An Experimental Study of Worthington Jet Formation after Impact of Solid Spheres. Massachusetts Institute of Technology.
Ou, Y.P., Dong, W.C., Xu, Y., 2010. Experimental study on the longitudinal motion performances of bottom hollowed high speed air cavity craft in regular wave. Shipbuild. China 51, 1–10.
Pan, G., Yang, K., 2014. Impact force encountered by water-entry airborne torpedo. Explos. Shock Waves 34 (05), 521–526.
Ramamurthi, K., Nandakumar, K., 1999. Characteristics of flow through small sharp-edged cylindrical orifices. Flow Meas. Instrum. 10, 133–143.
Savchenko, G.Y., 2012. Hydrodynamic Characteristics of a Disc with Central Duct in a Supercavitation Flow. Springer Berlin Heidelberg, Berlin.
Seddon, C.M., Moatamedi, M., 2006. Review of water entry with applications to aerospace structures. Int. J. Impact Eng. 32, 1045–1067.
Truscott, T.T., 2009. Cavity Dynamics of Water Entry for Spheres and Ballistic Projectiles. Massachusetts Institute of Technology.
Truscott, T.T., Techet, A.H., 2009. Water entry of spinning spheres. J. Fluid Mech. 625, 135–165.
Truscott, T.T., Epps, B.P., Belden, J., 2014. Water entry of projectiles. Annu. Rev. Fluid Mech. 46, 355–378.
Tseitlin, M., 1959. On the pressure on two parallel plates in a jet flow. TsAGI Trans. Hydrodyn. 296–308.
Von Karman, T., 1929. The Impact on Seaplane Floats during Landing. Naca Technical Report, p. 321.
Worthington, A.M., 1882. On impact with a liquid surface. Proc. R. Soc. Lond. 34, 217–230.
Wang, S., Guedes Soares, C., 2014. Numerical study on the water impact of 3D bodies by an explicit finite element method. Ocean Eng. 78, 73–88.
Zhao, Q., Chen, Z.H., Huang, Z.G., Zhang, H.H., Ma, J., 2019. Optimization of the aerodynamic configuration of a tubular projectile based on blind kriging. Sci. Iran. 26, 311–322.